Journal of Materials Chemistry A

ROYAL SOCIETY OF CHEMISTRY

PAPER

View Article Online
View Journal | View Issue

Cite this: J. Mater. Chem. A, 2017, 5, 14758

Ni/NiO nanoparticles on a phosphorous oxide/graphene hybrid for efficient electrocatalytic water splitting†

Juan Wang,[a] Yanan Xie,[a] Yuanying Yao,[a] Xing Huang, [b] Marc Willinger[b] and Lidong Shao *[a]

Received 27th April 2017
Accepted 20th June 2017

DOI: 10.1039/c7ta03628k

rsc.li/materials-a

Herein, Ni/NiO nanoparticles were anchored on phosphorous oxide/graphene for electrocatalytic water splitting. The organophosphate units in graphene nanosheets may facilitate the preferred formation of a surface oxide-modified nickel species with stable reduced electron density at the Fermi level. Efficient catalytic activity and stability in a hydrogen evolution reaction (HER) were obtained. Ni/NiO@HGP$_x$O$_y$ with a low nickel loading shows an overpotential of 205 mV at a current density of 10 mA cm^{-2} and a Tafel slope of 80 mV dec^{-1}, whereas those of its undoped counterpart are 278 mV and 117 mV dec^{-1}, respectively. We proposed that the small particle size, uniform dispersion of Ni/NiO nanoparticles, and electronic effect arising from the interactions between HGP$_x$O$_y$ and Ni/NiO nanohybrids contribute to the improved electrocatalytic performance.

Introduction

Hydrogen as a renewable energy carrier has attracted significant scientific interest since it does not cause carbon dioxide emission and is a good alternative to traditional fossil fuel.[1] Electrochemical water splitting is an effective and easy way of generating high-purity hydrogen.[2] Pt and its alloys are the most efficient electrocatalysts for hydrogen evolution reactions (HERs), but large-scale application of Pt-based catalysts is limited due to its scarcity and high cost.[3] As active and stable non-precious materials in alkaline solutions, Ni-based electrocatalysts have been commonly used for hydrogen generation.[4]

Recently, Ni/NiO heterostructures on oxygen-functionalized carbon nanotubes (OCNTs) have been used for HER from water electrolysis.[5] In this study, the OCNTs manipulated the formation of Ni/NiO through their interactions with nickel precursors. Compared to CNTs, graphene nanosheets with large surface area, excellent conductivity, and low thickness of the diffusion layer, which reduces the mass-transfer resistance, might be an astute choice as a support for the fabrication of these core–shell structured nanoparticles. In addition, better dispersion and smaller particle size can be obtained using graphene nanosheets as supports for active nanoparticles; moreover, during the synthesis process, graphene nanosheets suppress the aggregation of nanoparticles, which contributes to enhanced catalytic activity and stability.[6,7] Recently, Fe$_2$P/RGO sandwich-structured nanowall arrays have been reported as a non-noble-metal electrocatalyst for hydrogen evolution. Due to their maximally exposed catalytic sites and fast electron and mass transport, the arrays behave as a high-performance HER electrocatalysts.[8] Moreover, graphene facilitates electron transfer during the HER process; this induces ohmic loss of the catalytic system; thus, better catalytic current density is obtained.[9]

It is generally considered that dopants facilitate the initial nucleation of metal particles[10] and lead to a strong interfacial interaction between the carbon support and the metal particles.[11] Phosphorus has the same number of valence electrons as nitrogen and often displays similar chemical properties; however, it exhibits a stronger n-type behavior, making it a good choice for a carbon material dopant.[12,13] It has been reported that the electron-donating ability of the phosphorous oxide/graphene hybrid is superior to that of nitrogen-doped graphene,[14] indicating the catalytic potential of phosphorus doping.

To the best of our knowledge, there have been no reports on the fabrication of Ni/NiO on phosphorous oxide/graphene hybrid for HERs. Herein, we present the design and synthesis of highly dispersed Ni/NiO on a phosphorous oxide/graphene hybrid that provides a large number of anchoring sites. We proposed hybrids with modified electronic effects arising from the interactions between the surface-functionalized graphene nanosheets and Ni/NiO. In addition, the facile synthesis procedure involving deliberate thermal annealing that afforded

[a]Shanghai Key Laboratory of Materials Protection and Advanced Materials in Electric Power, Shanghai University of Electric Power, Shanghai 200090, PR China. E-mail: lidong.shao@shiep.edu.cn

[b]Department of Inorganic Chemistry, Fritz-Haber Institute of the Max Planck Society, Faradayweg 4-6, 14195 Berlin, Germany

† Electronic supplementary information (ESI) available: XRD, Raman, CVs and EIS characterizations. See DOI: 10.1039/c7ta03628k

partial reduction of nickel hydroxide could be easily scaled up for practical application.

Experimental

Preparation of the catalysts

Graphite oxide was prepared from purified natural graphite (SP-1, Bay Carbon) by Hummers method.[15] The graphene oxide nanosheets in water solution (0.5 g L^{-1}) were prepared after two-hour sonication. Lyophilization was performed to obtain highly dispersed oxides from the water solution. Then, heat treatment was performed under vacuum at 300 °C (constant pressure 4.5 × 10^{-4} torr). Subsequently, further heat treatments at 1000 °C in a flow of 25% H_2 mixed with He (total flow of 100 sccm) with and without sodium hypophosphite (NaH_2PO_2) were conducted to obtain P_xO_y incorporated graphene-based holey nanosheets (HGP_xO_y) and graphene-based holey nanosheets (HG), respectively. At last, the obtained sample was washed several times with distilled water and dried under vacuum at 60 °C. An impregnation-reduction method was used to prepare Ni/NiO@HGP_xO_y catalysts. $Ni(NO_3)_2\cdot 6H_2O$ and HGP_xO_y were dispersed in ethanol. Ni was loaded at 3 ± 0.2 wt%, measured by inductively coupled plasma (ICP). The impregnated material was appropriately hydrolysed to crystallise the precursors by decomposing the nickel precursor species in a tube furnace at 310 °C under a He atmosphere (total flow of 100 sccm). Furthermore, considering the fact that this decomposition condition might not be sufficient to obtain complete Ni/NiO core–shell hybrids, a second step of calcination was carried out at 400 °C in a flow of 25% H_2 mixed with He (total flow of 100 sccm) for further reduction to obtain Ni/NiO@HGP_xO_y. Finally, the sample was cooled down to room temperature under He, and the products were removed from the corundum tube. The details of the preparation procedures are shown in Fig. 1. The Ni/NiO@HG catalyst was synthesised in a similar way without the phosphorus doping procedure.

Chemicals

Potassium hydroxide (≥99.0%), nickel(II) nitrate hexahydrate (≥98.0%), sodium hypophosphite (≥97.0%), sodium hydroxide (≥97.0%), acetone (≥99.5%), HCl (35–37 wt%), Nafion solution (5 wt%), and methanol (≥95%) were bought from Aldrich Chemical Co. (USA). Pt/C (Johnson Matthey 20%) was purchased from Shanghai Hesen Co. (China).

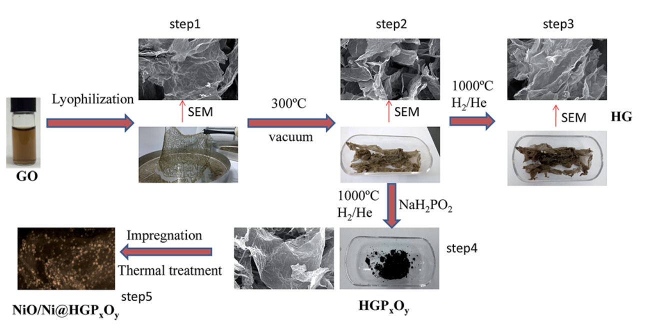

Fig. 1 Schematic of the design and preparation procedures of Ni/NiO@HGP_xO_y.

Characterization

Surface electronic states were analysed by X-ray photoelectron spectroscopy (XPS, PHI 5000 Versaprobe) with Al-Kα excitation. The binding energy scale was calibrated using the standard Au $4f_{7/2}$ and Cu $2p_{3/2}$ procedure. Core level spectra were obtained using a 30 eV pass energy. Inductively coupled plasma optical emission spectrometry (ICP-OES, PerkinElmer Optima 8000) was used for Ni content measurement in samples. An aberration-corrected JEOL JEM-ARM200CF transmission electron microscope (TEM) was employed to investigate the structural and chemical properties in the scanning TEM (STEM) mode. A Bruker DAVINCI D8 ADVANCE diffractometer with Cu-K_α radiation (λ = 0.15406 nm) was used for X-ray diffraction (XRD) characterization.

Electrochemical measurements

The electrochemical measurements of the catalysts were performed using a CHI 660E electrochemical workstation (CH Instruments, Shanghai, Chen Hua Co.) and a rotating disk electrode (RDE) (Pine Instruments, Grove City, PA) with a speed of 1600 rpm.

A standard three-electrode electrochemical cell was used. The counter and reference electrodes were graphite electrode and the Hg/HgO electrode, respectively. All potentials were quoted with respect to a reversible hydrogen electrode (RHE). The calibration (Fig. S1†) was performed in the high purity H_2 saturated electrolyte with a Pt wire as the working electrode. In 1 M KOH, E(RHE) = E(Hg/HgO) + 0.9305 V. Electrochemical impedance spectroscopy was performed when the working electrode was biased at a constant −0.20 V *vs.* RHE while sweeping the frequency from 100 kHz to 0.1 Hz with a 5 mV AC dither. The working electrode was a glassy carbon disk (5 mm in diameter), which was cleaned using deionized water and dried in air prior to the preparation of the catalyst layer on it. Briefly, the thin-film electrode was prepared as follows: 2.375 mg of catalyst was ultrasonically dispersed in 200 μL of ethanol and water mixture (ethanol : water = 4 : 1) with 20 μL of 5 wt% Nafion solution for 60 min. A 20 μL portion of catalyst ink (loading of 0.05 mg cm^{-2} for the active mass) was transferred onto the glassy carbon disk using a pipette and then dried in air.

Results and discussion

Composition and structural characterization

Graphene sheets remain holey structures with enriched defects and oxygen coverage even after high-temperature reduction treatments with phosphorus-containing precursors. A stack of basic structural carbon units with phosphorus oxides (P_xO_y) at the edges and internal defects was obtained. X-ray diffraction (XRD) patterns of line a in Fig. S2a† demonstrated that lyophilized GO with a diffraction peak at 2θ = 9.4° (interlayer distance 0.93 nm) was related to various oxygen-containing species and water molecules. Moreover, from the lines b–d, no diffraction peaks at 2θ = 21.6°, 43.3°, and 44.5° corresponding to 004, 100, and 101 planes can be found; this indicates that after vacuum annealing treatments, an amorphous turbostratic mixture of the structural units with internal lattice defects is formed.[16,17] As shown in the Raman spectra in Fig. S2b,† peaks at 1350 cm^{-1} (D band) and 1594 cm^{-1} (G band) can be observed, which result from the structural defects created by the attachment of hydroxyl and epoxide groups on the graphitic plane and the first-order scattering of the E_{2g} vibrational mode of graphitic structures, respectively. The I_D/I_G intensity ratio for both HG (line c) and HGP_xO_y (line d) after a 1000 °C heating process increases as compared to that for GO (line a and b), indicating that the reduction of GO induces increased internal lattice defects in holey structural units of HG and HGP_xO_y.

To determine the extent to which the vacuum and further annealing treatment restore the electrical properties of the graphitic network, the electrical conductivity of the materials obtained by steps 1–4 shown in Fig. 1 was measured using a digital four-point probe system. To obtain reliable electrical conductance data, ten different sites of each sample were measured. Moreover, the carbon to oxygen (C : O) ratios were deduced from the XPS data of the materials obtained from steps 1–4 shown in Fig. 1. Lyophilized GO with exfoliated-layer structures exhibits a conductivity of 6.82×10^{-4} S cm^{-1} and a C : O ratio of 4.93 : 1. Vacuum heating at 300 °C greatly enhanced the conductivity to 0.81 S cm^{-1}; however, the C : O ratio remained intact (4.97 : 1), indicating that vacuum heating at 300 °C did not remove the majority of oxygen-containing species. After reduction at 1000 °C under H_2/He, the conductivities of HG and HGP_xO_y were further improved (1.25 S cm^{-1} for HG and 1.27 S cm^{-1} for HGP_xO_y). These conductivity changes arise from the transformation of cyclic carbon oxides into a graphene SP2 network with multiple planar hexagonal aromatic rings. However, the C : O ratios were 12.4 : 1 for HG and 12.1 : 1 for HGP_xO_y, indicating the presence of oxygen species on the surfaces.

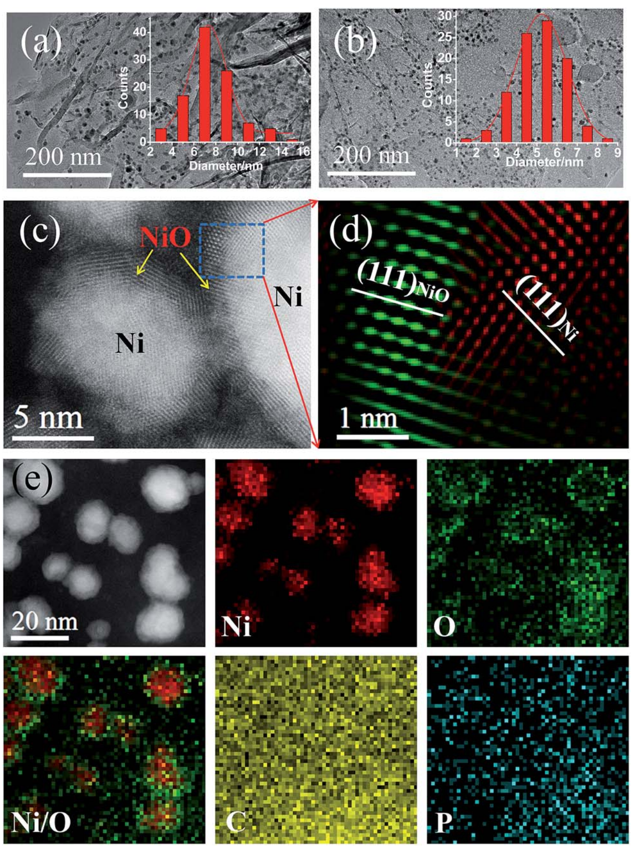

Fig. 2 TEM images and size distribution histograms of (a) Ni/NiO@HG and (b) Ni/NiO@HGP_xO_y. (c) and (d) HR-STEM images of Ni/NiO@HGP_xO_y, and (e) STEM images and EDX mappings of the Ni/NiO nanoparticles.

The structural and surface chemical properties of the catalysts were investigated by an aberration corrected JEOL ARM-200CF transmission electron microscope. TEM images revealed thin layers of graphene with wrinkles uniformly covered with nanoparticles. The particle sizes were estimated from the TEM images, with the size distribution histograms shown in Fig. 2a and b. The particle size range of Ni/NiO@HGP_xO_y particles was 2–9 nm, with an average size of 5.2 nm, whereas that of Ni/NiO@HG was 3–15 nm (average size: 7.6 nm). The narrow size distributions and smaller particle size of Ni/NiO@HGP_xO_y might originate from the P_xO_y incorporation. HR-STEM imaging results for Ni/NiO@HGP_xO_y are shown in Fig. 2c and d, and the marked lattice fringes correspond to the Ni(111) and NiO(111) crystal planes. STEM imaging and energy dispersive X-ray spectroscopy (EDX) mapping results for Ni/NiO@HGP_xO_y are shown in Fig. 2e, indicating the well-dispersed Ni/NiO core–shell structures with thin oxide layers of about 1.5 nm and a homogeneous distribution of C, N, O, and Ni in the catalyst. The Ni/NiO@HGP_xO_y nanoparticles were highly dispersed on the support surface and no aggregates were formed during the pyrolysis process, indicating a strong anchoring effect by HGP_xO_y. In the X-ray diffraction (XRD) patterns of the catalysts (Fig. S3†), the diffraction peaks at 44.5° and 43.3° correspond to the (111) plane of Ni (JCPDS no. 04-0850) and the (200) plane of NiO (JCPDS no. 47-1049).

To study the surface electronic properties of the catalysts, their surface chemical states were investigated by XPS. The P 2p XPS spectrum is shown in Fig. 3b. The lowest binding energy

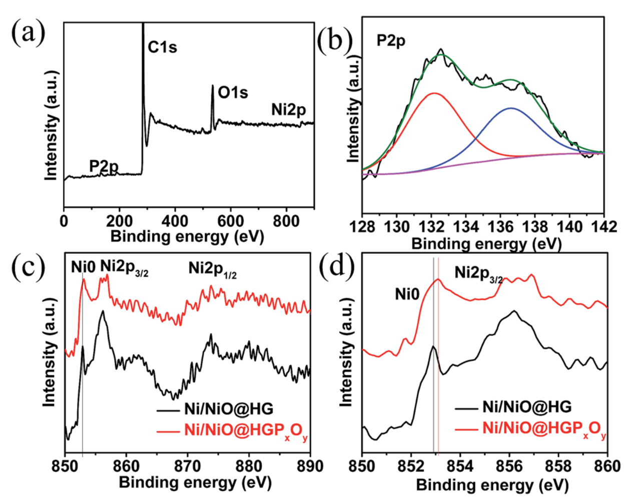

Fig. 3 (a) XPS survey of Ni/NiO@HGP_xO_y, deconvolution of (b) P 2p and (c) and (d) Ni $2p_{3/2}$ XPS spectra.

peak was at 132.2 eV, which represented oxidized P compounds,[18] and the peak around 133.6 eV was assigned to $(C_6H_5O)_3PO$ (P atom was bonded to four O atoms by one double bond and three single bonds).[19,20] This demonstrates that in this study, the doped phosphorous is mainly present in its oxidized form (P_xO_y). The Ni 2p spectra of the composites are shown in Fig. 3c and d. Arising from the multi-electron excitation, satellite peaks were also found along with the main peaks in the Ni 2p core-level spectra.[21] The Ni 2p peaks at around 852.7 ($2p_{3/2}$) and 869.8 eV ($2p_{1/2}$) indicate the presence of metallic Ni. Moreover, the Ni $2p_{3/2}$ peak around 855.8 eV and the Ni $2p_{1/2}$ peak around 873.5 eV indicate that Ni^{2+} is formed on the catalyst surfaces.[22,23] Compared with those of Ni/NiO@HG, the Ni 2p peaks of Ni/NiO@HGP_xO_y (Fig. 3d) were shifted to higher binding energies, which could be attributed to the interaction between Ni/NiO and HGP_xO_y, resulting in decreased electron density for Ni; this might affect the electrocatalytic activities in hydrogen evolution from water splitting.

Electrochemical properties of the catalysts

The HER catalytic performances of the Ni/NiO@HGP_xO_y nanohybrid were investigated in 1.0 M KOH at a scan rate of 5 mV s^{-1} using a three-electrode system with a rotating disk electrode (RDE) at 1600 rpm. Commercial Pt/C was investigated for comparison under the same active mass loading of Ni/NiO samples. IR corrections were conducted for all data for evaluating the intrinsic performance of catalysts. Linear sweep voltammograms (LSVs) for samples in 1.0 M KOH at a scan rate of 5 mV s^{-1} were obtained, and the results are shown in Fig. 4a. Note that graphene had negligible HER activity, whereas doping could significantly enhance the HER performance due to the generation of more active sites.[24] To achieve a 5 mA cm^{-2} HER current density in 0.1 M KOH solution, the phosphorus-doped graphene required an overpotential of 683 mV,[24] much higher than that of phosphorous oxide/graphene hybrid with Ni/NiO nanoparticles (160 mV). This suggested that after the introduction of Ni/NiO on doped graphene, more active sites for HER were generated. The curve for Ni/NiO@HGP_xO_y on a GC electrode with the active mass loading of 0.05 mg cm^{-2} indicated that an overpotential of 205 mV was required to obtain a current density of 10 mA cm^{-2}, whereas that required for Ni/NiO@HG and Pt/C was 278 mV and 72 mV, respectively. Moreover, a small onset potential of −30 mV was required for Ni/NiO@HGP_xO_y, whereas that required for Ni/NiO@HG was −60 mV. The catalytic activities of samples were further investigated by Tafel plots (Fig. 4b), and the linear regions were fitted into the Tafel equation. The Tafel slopes of Ni/NiO@HGP_xO_y and Pt/C are 80 and 35 mV dec^{-1}, respectively, whereas that of Ni/NiO@HG was much higher at 117 mV dec^{-1}, indicating favourable HER kinetics for P_xO_y incorporation. According to previous reports, Tafel slopes of phosphorus-doped graphene is 159 mV dec^{-1};[24] thus, the deposition of active Ni/NiO nanohybrids on HGP_xO_y also facilitated the HER process. The stability of the Ni/NiO@HGP_xO_y catalyst was evaluated by a chronoamperometry test (Fig. 4c) under an overpotential of 150 mV; after 3000 s, the current density changed from 3.70 mg cm^{-2} to 3.52 mg cm^{-2} and the polarization curves in Fig. 4d before and after 300 cycles CVs test in 1.0 M KOH at a scan rate of 50 mV s^{-1} showed a slight change in HER current density. Electrochemical double-layer capacitance was used to evaluate the electrochemical active surface area (ECSA) of Ni/NiO@HGP_xO_y and Ni/NiO@HG catalysts (Fig. S4†). We have performed cyclic voltammetry experiments for the catalysts in the range of 0.03–0.13 V *vs.* RHE at different scan rates to calculate the ECSA for both catalysts. The calculated C_{dl} for Ni/NiO@HGP_xO_y and Ni/NiO@HG are 0.00908 and 0.00408 mF cm^{-2}, respectively, and the number of active sites for both catalysts are calculated to be 1.0×10^{-3} mol g^{-1} and 0.47×10^{-3} mol g^{-1}. The Nyquist plots for Ni/NiO@HGP_xO_y and Ni/NiO@HG and the lines were fitted by an equivalent circuit in Fig. S5a and b,† respectively. Parameters such as the R_{ct} obtained by fitting the Nyquist plots to the equivalent circuit model are shown in Table S1.† R_{ct} is the charge transfer resistance at the electrolyte/catalyst interface, and the R_{ct} value for Ni/NiO@HGP_xO_y and Ni/NiO@HG are 51.3 and 112 Ω, respectively, indicating much faster charge transfer kinetics for Ni/NiO@HGP_xO_y.

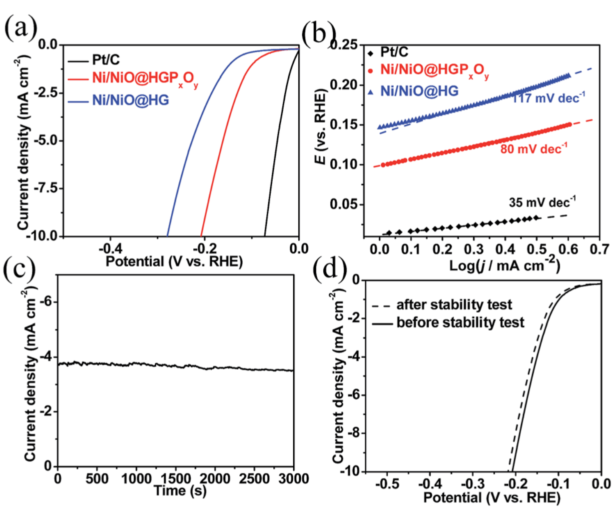

Fig. 4 (a) LSV curves for HER on catalysts, (b) Tafel plot derived from (a), (c) chronoamperometry test under an overpotential of 150 mV, and (d) polarization curves of Ni/NiO@HGP_xO_y before and after CVs tests for 300 cycles.

The mechanism for HER in alkaline solutions generally follows the Volmer–Heyrovsky or Volmer–Tafel process.[5,25]

$$H_2O + e \rightarrow H_{ads} + OH^- \text{ (Volmer)}$$

$$H_{ads} + H_{ads} \rightarrow H_2 \text{ (Tafel)}$$

$$H_2O + H_{ads} + e \rightarrow H_2 + OH^- \text{ (Heyrovsky)}$$

The generation and desorption of OH^- are related to both the Volmer and Heyrovsky steps. OH^- prefers to attach onto the Ni^{2+} (NiO) surface with more unfilled d orbitals and positive charge, and H^+ is prone to adsorb on the metal Ni surface. It is generally considered that H_2 is generated from the metal phase surface, and without NiO, the active metal phase site would be blocked by the occupation of OH^-. Thus, the co-existence of

NiO and Ni phases leads to a synergistic effect for hydrogen generation by electrocatalysis in alkaline solutions. The XPS study indicates that Ni in Ni/NiO@HGP$_x$O$_y$ has a positive shift, indicating that the electrons transfer from Ni to HGP$_x$O$_y$; thus, the positively charged Ni species and the negatively charged HGP$_x$O$_y$ act as the hydride-acceptor and proton-acceptor, respectively, to facilitate HER. Studies on metal phosphides have reported that the charge transfer usually occurs from the metal to P through the strong overlap between P and metal orbitals, and the phosphorus species could also affect the formation of nickel hydride in hydrogen generation by electrochemical desorption.[26] The use of a network of graphene-based nanosheets decreases the thickness of the diffusion layer and thereby reduces the mass-transfer resistance during electrocatalytic H_2 evolution process. P has the same number of valence electrons as N, but its larger atomic radius and greater electron-donating ability makes P an interesting choice as a dopant for C materials because it is expected to enhance their catalytic activity. When a heteroatom is introduced into the C framework, it creates defects in the nearby sites because of differences in bond lengths and atomic sizes and thus induces uneven charge distributions. P$_x$O$_y$ incorporation creates active sites for interactions with the nickel precursor and thus provides anchoring points for NPs formed during reduction.

Conclusions

In summary, for phosphorus doping, in this study, residual oxygen on carbon surfaces (graphene holes) may oxidize P(III) oxide and form a PO_4 organophosphate. Some P(III) oxide is left as a spectator. The PO_4 organophosphate units may facilitate the preferred formation of a surface oxide-modified nickel species with stable reduced electron density at the Fermi level. P$_x$O$_y$ holey graphene sheets were synthesised and used as a support material to assist the fabrication of Ni/NiO core–shell nanohybrids. The formation of Ni/NiO hybrids with synergistic effect of Ni (stabilize H atoms on Ni) and NiO (release generated OH^- on NiO) is beneficial for HER catalysis. Furthermore, this catalyst showed improved activity as compared to its non-doped counterpart. The incorporation of P$_x$O$_y$ changed the charge distribution of the catalyst, and the interactions between the Ni/NiO and HGP$_x$O$_y$ arising from charge transfer facilitated core–shell nanohybrid formation and thus enhanced the HER performance.

Acknowledgements

This work was financially supported by the Shanghai Key Laboratory of Materials Protection and Advanced Materials in Electric Power, the National Natural Science Foundation of China (21403137).

Notes and references

1 D. G. Nocera, The artificial leaf, *Acc. Chem. Res.*, 2012, **45**, 767–776.
2 M. G. Walter, E. L. Warren, J. R. Mckone, S. W. Boettcher, Q. Mi, E. A. Santori and N. S. Lewis, *Chem. Rev.*, 2010, **110**, 6446–6473.
3 Y. Sun, M. Delucchi and J. Ogden, *Int. J. Hydrogen Energy*, 2011, **36**, 11116–11127.
4 J. Cai, J. Xu, J. Wang, L. Zhang, H. Zhou, Y. Zhong, D. Chen, H. Fan, H. Shao, J. Zhang and C. Cao, *Int. J. Hydrogen Energy*, 2013, **38**, 934–941.
5 M. Gong, W. Zhou, M. C. Tsai, J. G. Zhou, M. Y. Guan, M. C. Lin, B. Zhang, Y. F. Hu, D. Y. Wang, J. Yang, S. J. Pennycook, B. J. Hwang and H. J. Dai, *Nat. Commun.*, 2016, **5**, 4695.
6 X. Huang, X. Qi, F. Boey and H. Zhang, *Chem. Soc. Rev.*, 2012, **41**, 666–686.
7 D. Chanda, J. Hnát, A. S. Dobrota, I. A. Pašti, M. Paidar and K. Bouzek, *Phys. Chem. Chem. Phys.*, 2015, **17**, 26864–26874.
8 M. J. Liu, L. M. Yang, T. Liu, Y. H. Tang, S. L. Luo, C. B. Liu and Y. X. Zeng, *J. Mater. Chem. A*, 2017, **5**, 8608–8615.
9 Y. G. Huang, H. L. Fan, Z. K. Chen, C. B. Gu, M. X. Sun, H. Q. Wang and Q. Y. Li, *Int. J. Hydrogen Energy*, 2016, **41**, 3786–3793.
10 B. Yue, Y. W. Ma, H. S. Tao, L. S. Yu, G. Q. Jian, X. Z. Wang, X. S. Wang, Y. N. Lu and Z. Hu, *J. Mater. Chem.*, 2008, **18**, 1747–1750.
11 Y. Shao, J. H. Sui, G. P. Yin and Y. Z. Gao, *Appl. Catal., B*, 2008, **79**, 89–99.
12 G. Wu, R. Swaidan, D. Li and N. Li, *Electrochim. Acta*, 2008, **53**, 7622–7629.
13 D. S. Yang, D. Bhattacharjya, S. Inamdar, J. Park and J. S. Yu, *J. Am. Chem. Soc.*, 2012, **134**, 16127–16130.
14 V. V. Strelko, V. S. Kuts and P. A. Thrower, *Carbon*, 2000, **38**, 1499–1503.
15 W. S. Hummers and R. E. Offeman, *J. Am. Chem. Soc.*, 1958, **80**, 1339.
16 T. F. Yeh, J. M. Syu, C. Cheng, T. H. Chang and H. Teng, *Adv. Funct. Mater.*, 2010, **20**, 2255–2262.
17 H. L. Wang, J. T. Robinson, X. L. Li and H. J. Dai, *J. Am. Chem. Soc.*, 2009, **131**, 9910–9911.
18 Z. W. Liu, Q. Q. Shi, F. Peng, H. J. Wang, R. F. Zhang and H. Yu, *Electrochem. Commun.*, 2012, **16**, 73–76.
19 J. F. Moulder, W. F. Stickle, P. E. Sobol and K. D. Bomben, *Handbook of X-ray photoelectron spectroscopy*, Perkin-Elmer Corporation, Eden Prairie, MN, 1992.
20 X. Wu and L. R. Radovic, *Carbon*, 2006, **44**, 141–151.
21 J. B. Wu, Z. G. Li, X. H. Huang and Y. Lin, *J. Power Sources*, 2013, **224**, 1–5.
22 L. L. Wang, D. F. Zhang and L. Guo, *Nanoscale*, 2014, **6**, 4635–4641.
23 Y. S. Li and Y. L. He, *RSC Adv.*, 2014, **4**, 16879–16884.
24 Y. Zheng, Y. Jiao, L. H. Li, T. Xing, Y. Chen, M. Jaroniec and S. Z. Qiao, *ACS Nano*, 2014, **8**, 5290–5296.
25 S. A. Vilekar, I. Fishtik and R. Datta, *J. Electrochem. Soc.*, 2010, **157**, B1040–B1050.
26 W. Zhang, J. D. Hong, J. W. Zheng, Z. Y. Huang, J. R. Zhou and R. Xu, *J. Am. Chem. Soc.*, 2011, **133**, 20680.